energies

MDPI

Article

Oxidized Nickel to Prepare an Inorganic Hole Transport Layer for High-Efficiency and Stability of $CH_3NH_3PbI_3$ Perovskite Solar Cells

Chien-Chung Hsu [1,†], Sheng-Min Yu [1,2,†], Kun-Mu Lee [3,4,5,*,†], Chuan-Jung Lin [1,†], Bo-Yi Liou [6] and Fu-Rong Chen [1,7,*]

1 Department of Engineering and System Science, National Tsing Hua University, Hsinchu 30013, Taiwan; benq211037@gmail.com (C.-C.H.); yushengmin@itri.org.tw (S.-M.Y.); chuanjung.lin@gmail.com (C.-J.L.)
2 Material and Chemical Research Laboratories, Industrial Technology Research Institute, Hsinchu 31040, Taiwan
3 Department of Chemical and Materials Engineering, Chang Gung University, Taoyuan 33302, Taiwan
4 Department of Pediatrics, Division of Neonatology, Chang Gung Memorial Hospital, Linkou, Taoyuan 33305, Taiwan
5 Green Technology Research Center, Chang Gung University, Taoyuan 33302, Taiwan
6 Department of Chemical and Materials Engineering, National Central University, Jhong-Li, Taoyuan 32001, Taiwan; p81309x@gmail.com
7 Department of Materials Science and Engineering, City University of Hong Kong, Hong Kong
* Correspondence: kmlee@cgu.edu.tw (K.-M.L.); frchen@me.com (F.-R.C.)
† These authors contributed equally to this work.

Abstract: In this study, we report a perovskite solar cell (PSC) can be benefited from the high quality of inorganic nickel oxide (NiO_x) as a hole transport layer (HTL) film fabricated from the physical vapor deposition (PVD) process. The power conversion efficiency (PCE) of PSC is found to depend on the thickness of NiO_x HTL. The NiO_x thickness is optimized via quantitative investigation of the structure, optical and electrical properties. With an active area of 11.25 cm^2, a PSC module (25 cm^2) with a PCE of 15.1% is demonstrated, while statistically averaged PCE = 18.30% with an open voltage (V_{oc}) 1.05 V, short-circuit current density (J_{sc}) 23.89 mA/cm^2, and fill factor (FF) 72.87% can be achieved from 36 devices with smaller active areas of 0.16 cm^2. After the stability test at 40% relative humidity (RH) and 25 °C for 1200 h, the highest performance NiO_x-based PSC is shown to be about 1.2–1.8 times superior to PEDOT:PSS organic HTL based PSC at the same environment.

Keywords: hole transport layer; perovskite; stability; reliability; power conversion efficiency

Citation: Hsu, C.-C.; Yu, S.-M.; Lee, K.-M.; Lin, C.-J.; Liou, B.-Y.; Chen, F.-R. Oxidized Nickel to Prepare an Inorganic Hole Transport Layer for High-Efficiency and Stability of $CH_3NH_3PbI_3$ Perovskite Solar Cells. *Energies* **2022**, *15*, 919. https://doi.org/10.3390/en15030919

Received: 7 December 2021
Accepted: 17 January 2022
Published: 27 January 2022

1. Introduction

Organic–inorganic hybrid perovskite is a very potential material in many application fields, such as organic light-emitting diodes (OLED) [1,2], thin-film transistors (TFT) [3], photodetector [2–4], and photovoltaic solar cells [5]. The PCE of organic–inorganic hybrid photovoltaic perovskite solar cell devices has been improved from 3.8% to over 25.5% within recent years [1–6]. The photoactive layer $CH_3NH_3PbI_3$ has a direct bandgap of around 1.5 eV (300–800 nm) with a long carrier diffusion length (>1 μm) [7]. However, the light absorption of a hybrid perovskite can cover visible regime (400–800 nm) with a high extinction coefficient (~10^4 cm^{-1} at 550 nm) [8]. The perovskites materials have a crystal structure similar to ABX_3. [2–6]. The symbol A is monovalent cation: Methylammonium (MA^+), Formamidinium (FA^+), and Cesium (Cs^+); B is divalent metal cation: Tin (Sn^{2+}) and Lead (Pb^{2+}) and X is halide anion: Iodine (I^-) or Bromine (Br^-), respectively [2–8]. One of the most attractive points for scientists is that these perovskite materials can be synthesized in a low-temperature process with low manufacturing cost that makes the future application more affordable. Usually, a hybrid perovskite solar cell has an inverted (p-i-n structure) configuration given as followed: hole transport layer (HTL)/$CH_3NH_3PbI_3$/electron transport

layer (ETL). In this configuration, the perovskite absorber layer connects to both the HTL and ETL. In an inverted (p-i-n structure) photovoltaic solar cell device, the ETL material must be prepared at the low-temperature process that prevents damaging the perovskite layer. Usually, the solution process 6,6-phenyl C61-butyric acid methyl ester (PCBM) (refs) and evaporated C60 are the most widely used to ETL. However, the disadvantages to PCBM were current leakage, lower electron mobility, and charge recombination with perovskite at the interface [4]. As compared to PCBM, the C_{60} can be more uniformly cover onto perovskite, which increased electron transport. The performance for inverted (p-i-n structure) PSC with C_{60} is better than PCBM based for photovoltaic devices. Moreover, the C_{60} material can be fabricated in either solution process or vacuum thermal evaporation. The vacuum thermal evaporation is applicable for large area fabrication for the ETL layer. In this aspect, the evaporate C_{60} material is the most widely used to ETL [5,9].

While for HTL, the poly (3,4-ethylene dioxythiophene) poly (styrene-sulfonate) (PEDOT:PSS) is usually used [10,11] as the key materials. The PEDOT:PSS has good conductivity (450 S/cm) and optical transmittance in the visible wavelength range (400–800 nm) [3,10–12]. However, the PEDOT:PSS solution is usually acidic. The PEDOT:PSS can cause indium (In) migration into the PEDOT:PSS layer and therefore damage the indium tin oxide (ITO) electrode. In addition, perovskite material basically contains methylamine that can actively react with acid PEDOT:PSS [4,9–12]. Besides, the PEDOT:PSS material was hygroscopic that damages the interface, and causes a mismatch in work function. Therefore as a role of HTL, the poor stability, high process cost, acidity, and hygroscopicity limit the practical application of PEDOT:PSS on large scale solar devices. In addition, matching the work function of traditional PEDOT:PSS and that of lead iodide-based perovskite greatly set a constraint to the electrical properties of hybrid perovskite solar cells, especially the open-circuit voltage (V_{OC}), which is usually lower than 1.0 V [12].

Compared with HTL made of organic materials, inorganic p-type semiconductors can provide inherently higher stability. As a role of HTL, p-type inorganic (NiO_x) has been extensively studied [11–13] due to it has wide bandgap (Eg > 3.5 eV) [14–17], high optical transmittance [18–22], good chemical stability, and an appropriate valence band [23–25] better matching with that of $CH_3NH_3PbI_3$ as compared with (PEDOT:PSS) [26–28]. Besides, NiO_x has better hole mobility of 2.8 cm^2/Vs [29], as compared with NiO_x, the PEDOT:PSS is about 1.5 cm^2/Vs [30]. NiO_x has a highly stable crystal structure that can be prepared by various methods, such as sol-gel [18], electrodeposition [19], spray pyrolysis [30], spin coating [13,24], pulsed laser deposition [31]. The advantages of the sputtering process, are high deposition rate, films uniformity, large area, and reproducibility as compared to the solution process. Therefore, NiO_x can be a very potential application for perovskite solar cells as an HTL [21,23,32]. Furthermore, due to the fact that C_{60} possesses much higher electron mobility (1.6 cm^2/Vs) and conductivity (2.3 $\times$ 10^{-3} S/cm) than those spin coated PCBM (6.1 $\times$ 10^{-2} cm^2/Vs and 3.2 $\times$ 10^{-4} S/cm), respectively [33], recently C_{60} and BCP deposited by vacuum thermal evaporation are more frequently accepted as a preferable ETL [10].

To improve the sustainability and the performance of perovskite solar cells, the organic ETL PCBM, and HTL PEDOT:PSS in an inverted configuration (pin, HTL/ $CH_3NH_3PbI_3$/ETL) of hybrid perovskite cell, are replaced with the inorganic C_{60} and NiO_x, respectively. In this study, we have fabricated highly efficient inverted (p-i-n structure) perovskite solar cell devices with inorganic HTL and ETL with stackings: FTO/NiO_x/$CH_3NH_3PbI_3$/C_{60}/Bathocuproine (BCP)/Ag. It was reported that the PCEs of perovskite cells composed of solution-coated HTL NiO_x on ITO had been demonstrated to be as high as 5.7% and 15% [11,13]. In this study, we have optimized NiO_x thickness by quantitatively analyzing its structure, optical and electrical properties. We fabricated 36 devices of perovskite solar cells for reproducibility tests under AM 1.5G illumination. It was demonstrated that the device has an averaged V_{oc} = 1.05 V, J_{sc} = 23.89 mA/cm^2, FF = 72.87%, and PCE = 18.3% from an active area of 0.16 cm^2. The durability test showed the lifetime of our perovskite cell can be as long as 1200 h which benefits from a follow-up annealing at high temperature

after NiO_x is deposited onto a FTO substrate. This follow-up annealing is critical to guarantee a high-quality NiO_x film to reach PCE = 18% (active area of 0.16 cm^2) and 1200 h lifetime. Furthermore, with the integration of the sputtering process for NiO_x, this proposed structure inorganic HTL/$CH_3NH_3PbI_3$/inorganic ETL can be integrated to be a large scale and sheet-to-sheet process for perovskite solar cells.

2. Experimental and Methods

2.1. Device Structure and Fabrication

Our inverted (p-i-n structure) planar heterojunction perovskite device has a stacking structure shown in Figure 1: FTO/NiO_x/$CH_3NH_3PbI_3$/C_{60}/BCP/Ag. The films of the perovskite device were deposited sequentially as its stacking structure. Two different sizes of devices with an active area of 0.16 cm^2 and 11.25 cm^2, respectively, were fabricated by the following procedures. Fluorine-doped tin oxide (FTO; 15 Ω/sq^1) glass substrates were cleaned with ultra-sonication for 20 min in detergent water, acetone, and isopropanol, sequentially. Then FTO glass was baked for 1 h at 150 °C to remove moisture. After that, the FTO glass was placed in UV-ozone for 20 min.

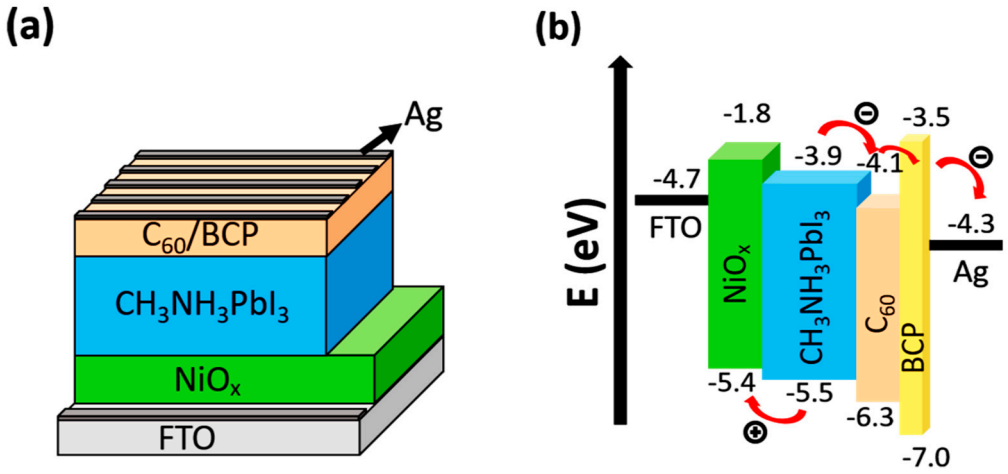

Figure 1. The perovskite solar cell device: (**a**) Inverted (p-i-n structure) configuration; (**b**) the energy level diagram of the working principle.

The NiO_x films were deposited onto the FTO glass for several lengths of time (20 s–80 s) by the RF magnetron sputtering method. The nickel target has a size of 2″ and has a purity of 99.99%. The target and the substrate were set to be approximately 8 cm apart in the sputtering chamber which was evacuated to a base pressure below 5×10^{-6} torr before deposition. The power is set to be 200 W, and four film thicknesses were controlled with deposition time set for 20 s, 40 s, 60 s, and 80 s, respectively. NiO_x film was formed by annealing the as-deposited nickel film in a quartz tubular oven for 1 h at 500 °C with an oxygen flow of 60 sccm. The solution for preparation of light absorber layer the perovskite layer is a 1.5 M methylammonium lead tri-iodide ($MAPbI_3$) solution, that contains 0.578 g of lead iodide (PbI_2, 99.9985%, Alfa Aesar, Hefreer, MA, USA) and 0.196 g methylammonium iodide (MAI) which is dissolved into a mixed solvent containing Dimethyl sulfoxide (DMSO, ≥99.9%, Sigma-Aldrich, St. Louis, MO, USA) and Gamma-Butyrolactone (GBL, ≥99%, Sigma-Aldrich) (DMSO: GBL, 1: 1 volume ratio). This solution was then oscillated and heated at 50 °C for 3 h in an ultra-sonication process. Then the perovskite layer was spin coated onto the NiO_x film layer with the one step process that without an anti-solvent wash procedure involved in a nitrogen glove box.

The substrate of FTO/NiO_x was baked at 120 °C for 10 min with a hot plate then it was treated in UV-ozone for 15 min. The perovskite film was fabricated by spin coating with $MAPbI_3$ solution at 1000 rpm for 10 s then 3000 rpm for the 30 s. Perovskite film with a thickness of about 340 nm was formed after the sample is baked at 100 °C for 10 min

with a hot plate. Followed, thin layers of C_{60}/BCP with thicknesses of 45 nm and 5 nm, respectively, were deposited onto perovskite film. The C_{60} and BCP are deposited by a process of vacuum thermal evaporation. Finally, silver contact is deposited onto the BCP by the thermal evaporator under a vacuum chamber with a base pressure of 5×10^{-6} torr for device fabrication. The thickness of the silver electrode is about 100 nm. The active area of two sets of perovskite devices was made to be around 0.16 cm^2 and 11.25 cm^2, respectively, which was defined with a shadow mask during Ag evaporation. The construction of inverted (p-i-n structure) PSCs is shown in Figure 1a and the energy level of the working principle for inverted perovskite ($CH_3NH_3PbI_3$) solar cell devices is shown in Figure 1b.

2.2. Equipment Specification

The ex-situ X-ray diffraction patterns were recorded on a high resolution X-ray diffractometer equipped (Bede D1) with Cu-kα that operate conditions are 45 kV and 35 mA, radiation at a scanning rate of 2 °/min. The optical transmittance spectra of NiO_X films was recorded with an ultra violate visible (UV-vis) spectrometer (LAMBDA 900, PerkinElmer, Waltham, MA, USA). The surface morphology and cross-section structure used a high-resolution field emission scanning electron microscope (FE-SEM, JSM-7610F, JEOL Ltd., Tokyo, Japan). The wavelength of Photoluminescence (PL) (Agilent Technologies, Santa Clara, CA, USA) excitation was set to be 633 nm. Hall Effect measurement was investigated using nanometrics HL5500. The ultraviolet photoelectron spectroscopy (UPS, Atlanta, GA, USA, PHI 5000 Versaprobe II, ULVAC-PHI) of the He source is used to measure the work function. High-resolution transmission electron microscope (HRTEM) was used to observe crystal structure and energy dispersive X-ray spectrometer (EDS) was applied to map for elemental distribution (FE-TEM, JEM-2010F, JOEL). TEM sample was cut and thinned with a dual beam focused ion beam (FIB, Helios 1200^+, FEI, Lausanne, Switzerland). Under 1 sun illumination (100 mW/cm^2, AM 1.5G), a computer-controlled digital source meter (Keithley 2400, Cleveland, OH, USA) was used to measure the current density and voltage (J-V) curves characteristic. The light power of a solar simulator (Oriel Sol3A class AAA, Newport Corporation, Irvine, CA, USA) was set to be 450 W. Before each measurement, an NREL-certified silicon solar cell (Oriel 91150V) with a KG-5 filter was used to calibrate light intensity [34]. The PCE scan was set to start from 1.2 to −0.2 V, then the scan rate of voltage was fixed at 50 mV/s.

3. Results and Discussion

The work functions of FTO, NiO_x, $CH_3NH_3PbI_3$, C_{60}, BCP, and Ag are also given in Figure 1b. When the light irradiates onto an absorber layer of the $CH_3NH_3PbI_3$ film, the electrons were pumped from the valence band to the conduction band. Immediately, the electrons transport to the electron transport layer (ETL) of the n-type C_{60}, while the holes transport to HTL of the NiO_x layer. The C_{60} has a lower work function (−4.1 eV) which matches with the lowest unoccupied molecular orbital (LUMO) energy level of perovskite film (LUMO = −3.9 eV). The band structure of $CH_3NH_3PbI_3/C_{60}$ further accelerates the electron transport to the silver cathode (LUMO = −4.3 eV). To effectively guide holes, the work function of p-type NiO_x (−5.4 eV) must be matched as much as possible with the Highest Molecular Orbital (HOMO) energy level of the FTO (HOMO = −4.7 eV). In order to avoid annihilation of a hole with an electron at the Ag electrode, the BCP is used to prevent hole transmission to the silver cathode, avoid electron and hole recombination at the interface while the p-type NiO_x prevents the electron injection into the anode to affect the efficiency of the hole.

Figure 2a the NiO_x films prepared for various deposition times: 20 s, 40 s, 60 s, and 80 s, respectively, were annealed at 500 °C for 1 h. The equivalent thicknesses of these films are 25 nm, 50 nm, 75 nm, and 100 nm, respectively. Figure 2b shows the UV-vis transmission spectra of the NiO_x layer as a function of wavelength in the range (350~800 nm). All NiO_x films have transmittance higher than 70% for wavelength longer than 400 nm. For 20 s and 40 s cases, the transmission even exceeds above 90%. Besides,

the double layer and different pyramid period textures can increase transmission in the shorter wavelength. The high transmittance of NiO_x films benefits the characters of being HTL due to the fact that the light can efficiently transport to FTO/NiO_x/$CH_3NH_3PbI_3$ for decreased quantum efficiency (QE) losses, which improve short-circuit current density (J_{sc}) and energy conversion efficiency [35–37].

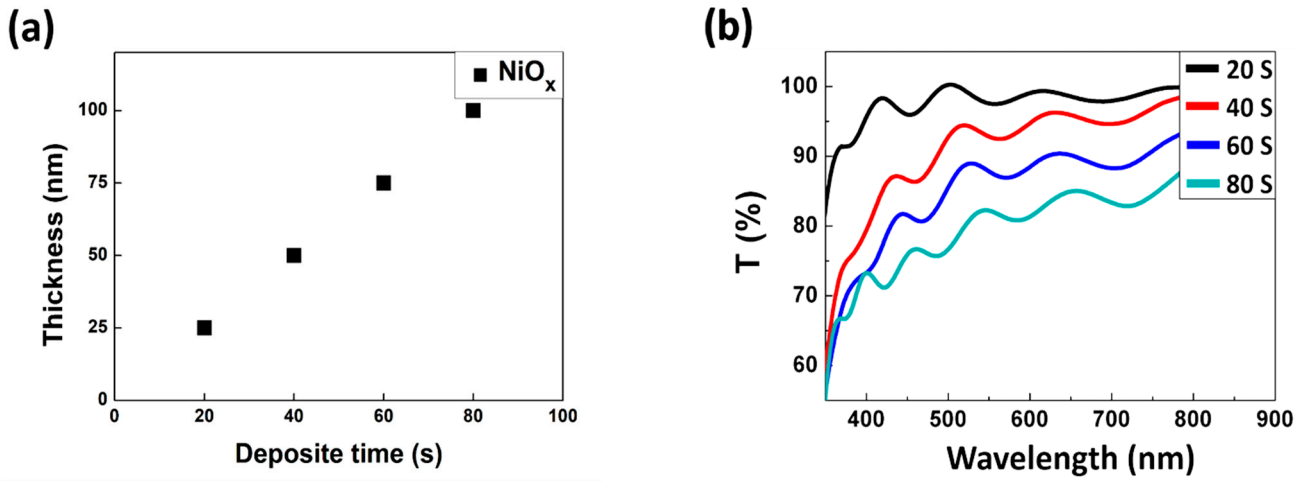

Figure 2. NiO_x films prepared to various deposit times: (**a**) from deposit times: 20 s, 40 s, 60 s, and 80 s, respectively, were annealed at 500 °C for 1 h. The equivalent thicknesses are 25 nm, 50 nm, 75 nm, and 100 nm, respectively; (**b**) transmittance vs. wavelength (350–900 nm) for various NiO_x thin films.

X-ray diffraction (XRD) patterns of various NiO_x layers are shown in Figure 3a. It is worth noting that the NiO_x diffraction peaks can be observed when deposition time: 20 s, 40 s, 60 s, 80 s, respectively. The crystallinity of NiO_x films becomes better with increase of deposition time. Figure 3a show the XRD patterns of NiO_x films processed for various lengths of time with the θ–2θ (GIXRD) scan from 30° to 50°. Noted that only $(111)_{NiOx}$, and $(200)_{NiOx}$, at around 37° and 43°, are shown respectively (JCPDs card #73-1523). The $CH_3NH_3PbI_3$ thin film was grown on NiO_x substrate. There are several peaks (Figure 3b) at 14.08°, 20.8°, 23.51°, 24.55°, 28.4°, 31.86°, and 35.06°, respectively. These peaks correspond to the (110), (200), (211), (202), (220), (310), and (312), respectively, lattice planes of tetragonal $CH_3NH_3PbI_3$ crystal. These peaks are in good agreement with those reported in earlier publications (JCPDs card #07-0235). XRD provides strong evidence for confirmation of the pristine crystal of NiO_x and perovskite.

Figure 4a shows the surface microstructure and morphology of various thicknesses of NiO_x HTLs processed at different deposition times. Obviously, all the NiO_x HTLs uniformly cover the FTO surface without pinholes. We can observe the NiO_x grain size increases as the sputter deposition time (20–80 s) increases. As a result, the resistivity of the NiO_x films layer decreases since the area of grain boundary reduces. Here, the NiO_x HTL is also known as the electron blocking layer, which can prevent intimate contact between the $CH_3NH_3PbI_3$ and the FTO. Therefore, the NiO_x layer can prohibit e-h charge recombination at the interface. A typical cross-sectional view for the inverted (p-i-n structure) perovskite solar cell NiO_x/$CH_3NH_3PbI_3$/C_{60}/BCP/Ag is clearly shown in Figure 4b. All layers show uniform thickness without any pinhole. The thickness of each NiO_x HTL layer is measured to be 50 nm, 340 nm, 50 nm, and 100 nm, respectively.

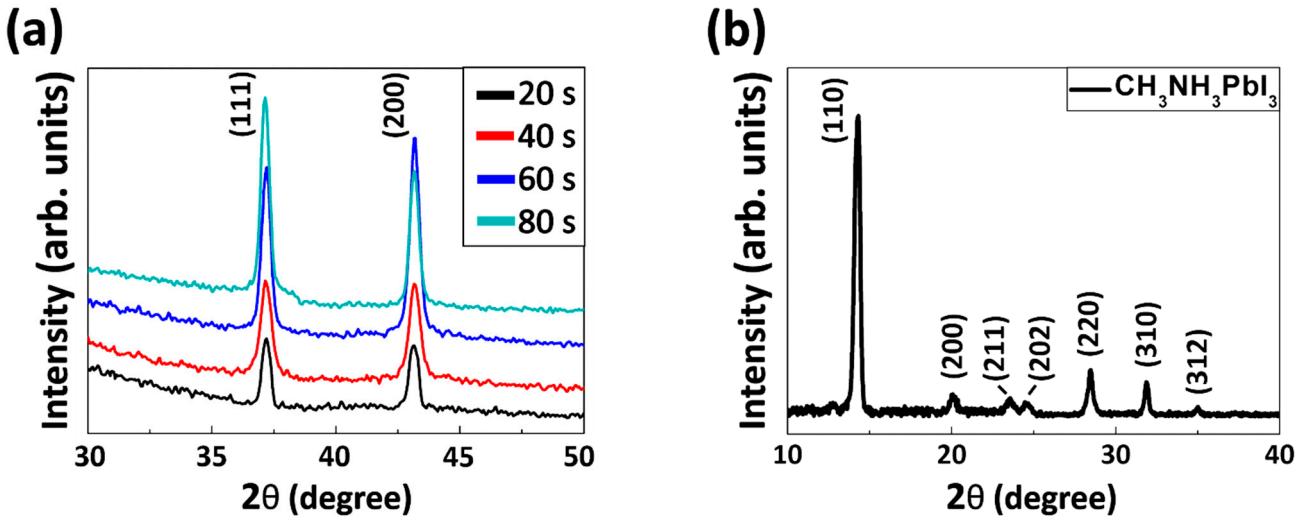

Figure 3. The XRD diffraction patterns show: (**a**) NiO_x hole transport layers deposited times for 20 s, 40 s, 60 s, and 80 s, respectively. All NiO_x films were annealed at 500 °C for 1 h; (**b**) the XRD diffraction peak of a $CH_3NH_3PbI_3$ perovskite film.

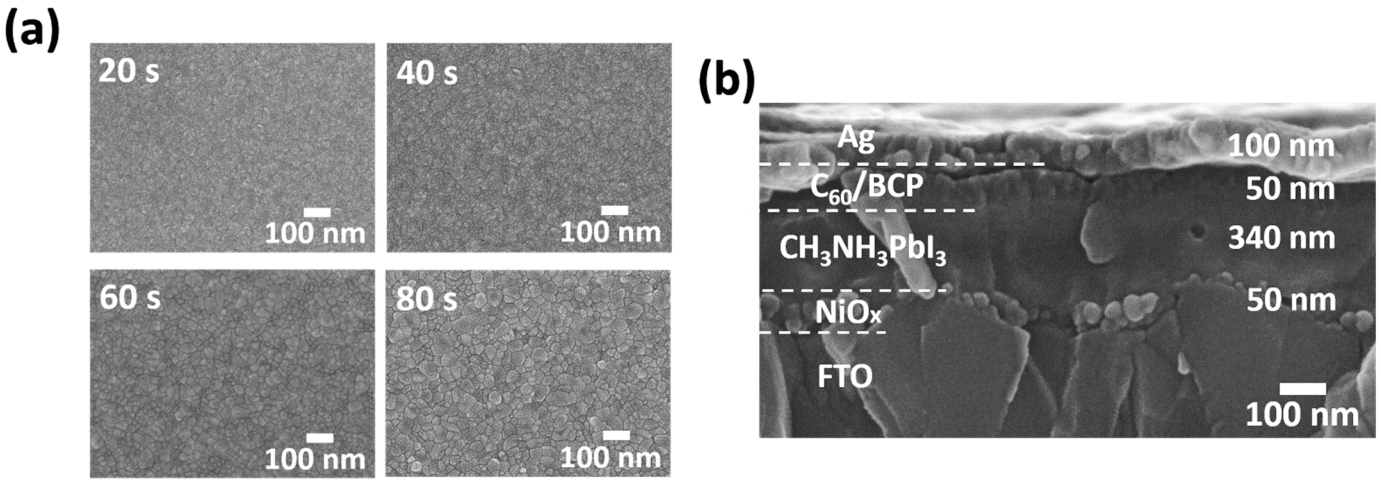

Figure 4. SEM images show surface morphology of various NiO_x films on FTO substrate: (**a**) from top-view: disposition time: 20 s, 40 s, 60 s, and 80 s, respectively. These samples were annealed at 500 °C for 1 h; (**b**) cross-sectional view of a perovskite solar cell device with stacking sequence of FTO/NiO_x/$CH_3NH_3PbI_3$/C_{60}/Bathocuproine (BCP)/Ag (both scale bars are 100 nm).

The HRTEM magnified image of NiO_x (deposit = 40 s) and $CH_3NH_3PbI_3$ film are given in Figure 5a. The crystal structures of NiO_x and $CH_3NH_3PbI_3$ phases can be confirmed from the Fourier transformed (FT) patterns of local atomic resolution images from the area enclosed in a white dotted line rectangular box (Figure 5a). From the FT patterns, we see NiO_x and $CH_3NH_3PbI_3$ are cubic structures and tetragonal structures, respectively. The elemental distribution of Ni (blue), Pb (red), O (yellow), and I (green) are presented in form of EDS maps of NiO_x and $CH_3NH_3PbI_3$ in Figure 5b.

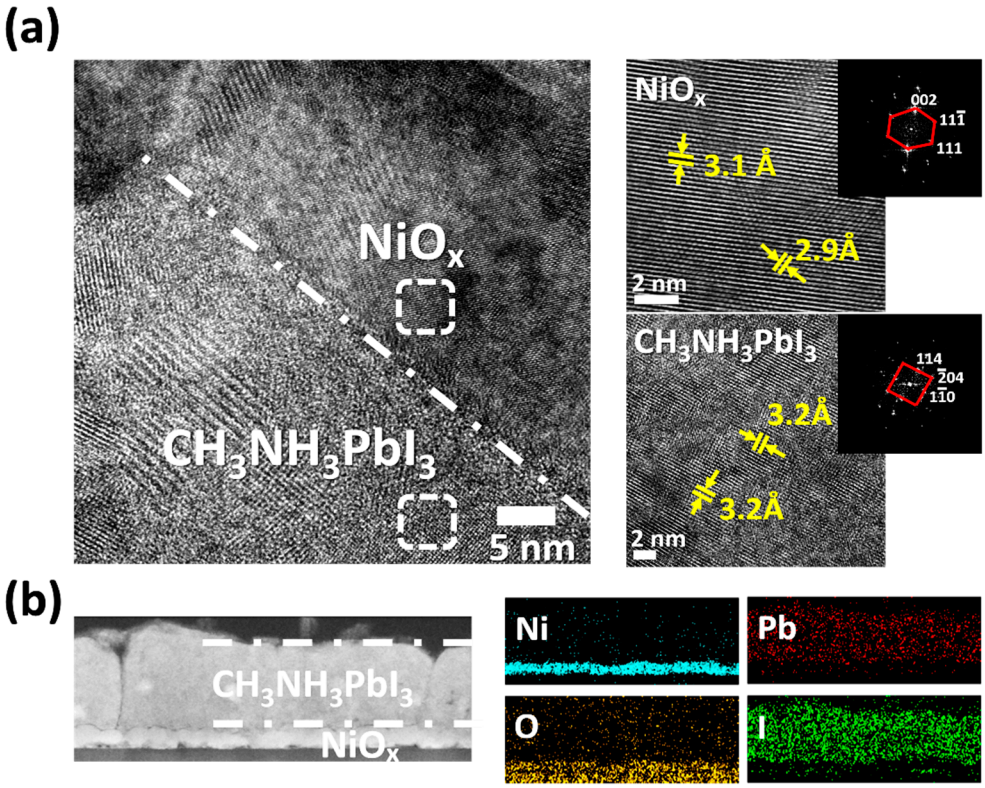

Figure 5. HRTEM image shows the crystal structure of $NiO_x/CH_3NH_3PbI_3$ films: (**a**) the $NiO_x/CH_3NH_3PbI_3$ films (scale bar is 5 nm). The dashed box areas of NiO_x and $CH_3NH_3PbI_3$ are shown as magnified views in the right-hand side (scale bar is 2 nm). Inset are FT patterns. The zone axis of NiO_x (top): $[110]_{cub}$, $CH_3NH_3PbI_3$ (bottom): $[221]_{tet}$. (**b**) EDS maps show the elemental distribution of Ni (blue), Pb (red), O (yellow), and I (green) of $NiO_x/CH_3NH_3PbI_3$.

The PL spectrum from $FTO/NiO_x/CH_3NH_3PbI_3$ can independently offer information of the structure and performance of cell PCE. In this study, $CH_3NH_3PbI_3$ is coated on various thicknesses (25–100 nm) of NiO_x HTL on bare glass. As a 633 nm laser is pumped onto the $FTO/NiO_x/CH_3NH_3PbI_3$ samples, an emission wavelength is expected to be detected at around 755 nm (Figure 6), which corresponds to a direct bandgap emission from first conduction band to first valence band of $CH_3NH_3PbI_3$. The quenching of electron-hole pairs at the interface can be evaluated from relative PL intensity. Between the NiO_x hole transport layer and the $CH_3NH_3PbI_3$ layer. Since the laser enters from NiO_x layer before $CH_3NH_3PbI_3$ layer, the exciton quenching efficiency can be affected by the thickness of NiO_x thin films. The relatively lower PL intensity represents higher quench efficiency [38,39] related to the fast hole mobility in NiO_x layer such that the recombination of e-h in $CH_3NH_3PbI_3$ layer is reduced. Compared to other deposition times, the NiO_x film processed for 20 s (thickness = 25 nm) has lower efficient carrier extractions. Due to the work function mismatch with perovskite and the lower carrier mobility. Figure 6 shows the relative intensity of the PL signal has a positive dependence on the thickness of NiO_x layer. It is obvious that NiO_x film deposited for 40 s (thickness = 50 nm) shows the lowest PL intensity, which indicates that this NiO_x layer collects holes with the highest efficiency, due to the fact hole mobility of NiO_x films is thickness dependence. The higher PL signal may indicate that the electron-hole pair is relatively more difficult to be separated and collected at $CH_3NH_3PbI_3/NiO_x$ interface. In addition, the work function measurement by UPS of the various thicknesses of NiO_x films: 20 nm, 40 nm, 60 nm, and 80 nm are −5.1 eV, −5.4 eV, −5.3 eV, −5.2 eV, respectively. The NiO_x films processed for 40 s (thickness = 50 nm) gives relative work function (HOMO = −5.4 eV) matches with that of the perovskite (HOMO = −5.5 eV). It is well-known, as the thickness increases in NiO_x layer, the decrease in series resistance (Rs). The resistivity and mobility of the various thickness NiO_x films

(25–100 nm) are measured by the Hall Effect. The resistivity were 5.2 × 10^{-4} Ω/cm, 3.8 × 10^{-4} Ω/cm, 2.6 × 10^{-4} Ω/cm, and 1.4 × 10^{-4} Ω/cm, respectively. This is consistent with the grain size result shown in the SEM experiment (Figure 4a), and that the carrier mobilities were 0.27 cm^2/Vs, 0.43 cm^2/Vs, 0.51 cm^2/Vs, and 0.54 cm^2/Vs, respectively. It will be shown later this thickness dependent quenching effect will also be consistently evidenced in a systematical PCE test.

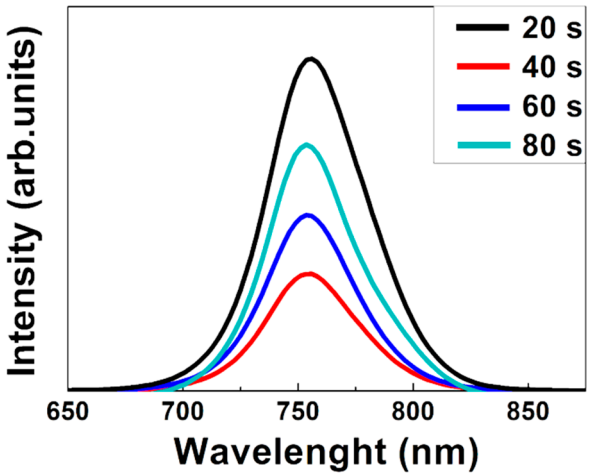

Figure 6. PL spectrum for $CH_3NH_3PbI_3$ perovskite film onto FTO/NiO_x hole transport layers treated at various deposition times: 20 s, 40 s, 60 s, and 80 s, respectively.

Based on the above results, inverted (p-i-n structure) perovskite devices are prepared. The photovoltaic performance (Figure 7a) for a device composed of NiO_x/$CH_3NH_3PbI_3$ perovskite film processed for 40 s (thickness = 50 nm) is shown. A typical J_{sc}-V_{oc} curve and a table in Figure 7a shows the campion values of V_{oc} = 1.05 V, J_{sc} = 23.89 mA/cm^2, FF = 72.87%, and PCE = 18.3%, which gives an averaged PCE = 17.1% for 36 devices (under AM 1.5G illumination). The statistic PCE from 36 devices are given as an inset (red bar chart) with an active area of 0.16 cm^2. A statistic table from the red bar chart shows averaged values and standard error (STD) of V_{oc}, J_{sc}, FF, and efficiency of 36 devices. In the module (25 cm^2), we demonstrate a perovskite device (active area 11.25 cm^2) the parameters of the V_{oc} = 4.55 V, short circuit current (I_{sc}) = 40.81 mA, J_{sc} = 4.31 mA/cm^2, and FF = 77% with an efficiency of 15.1% (Figure 7b). Figure 7c shows the consistent result that has been evidenced in the PL experiment (Figure 6). We observed that a 40 s deposit (thickness = 50 nm) is found to have the highest PCE since it had the best quench efficiency as suggested from the PL experiment. The efficiency of deposit NiO_x films at 20 s (thickness = 25 nm), 40 s (thickness = 50 nm), 60 s (thickness = 75 nm), and 80 s (thickness = 100 nm) that 6.8%, 18.3%, 14.8%, 12.3%, respectively.

Compared the long-term perovskite device stability of $CH_3NH_3PbI_3$ perovskite photovoltaic cells fabricated for the PEDOT:PSS and NiO_x HTLs (thickness = 50 nm) (Figure 8). The durability test is carried out at RH = 40% and 25 °C. In general, the efficiency of perovskite solar cell devices with NiO_x HTL is about 1.2 to 1.8 times superior to that with PEDOT:PSS. After 1200 h test, the $CH_3NH_3PbI_3$ perovskite photovoltaic cells fabricated from NiO_x and PEDOT:PSS decays 15.0% and 40.9% of their initial efficiencies, respectively.

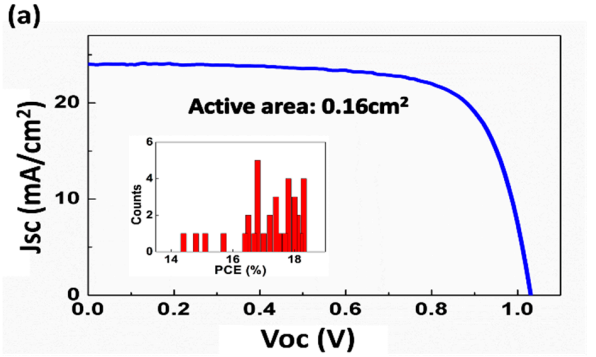

	Voc (V)	Jsc (mA/cm²)	F.F	Efficiency (%)
Champion	1.05	23.89	0.73	18.30
Avg.	1.04	22.88	0.72	17.13
STD.	0.01	1.07	1.23	0.98

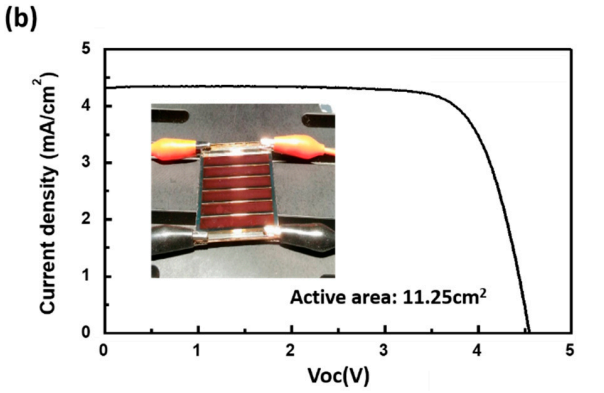

I_{SC} (mA)	J_{SC} (mA/cm²)	V_{OC} (V)	FF	Efficiency (%)
40.81	4.31	4.55	0.77	15.1

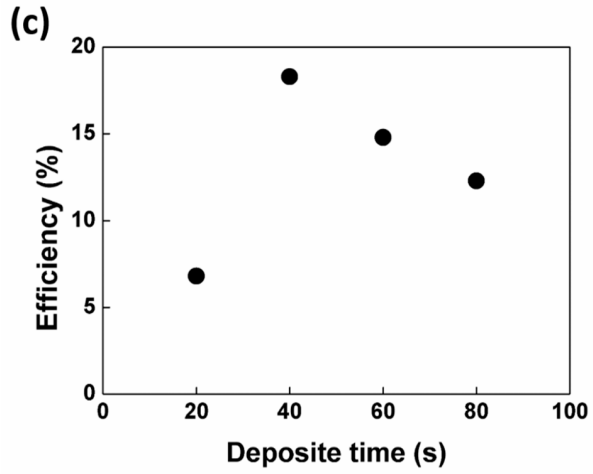

Figure 7. J_{sc}-V_{oc} curve and PCE related parameters of the perovskite device: (**a**) the statistic PCE from 36 devices are given as an inset (red bar chart). The average efficiency is 17.13%. A table shows averaged values and standard error of V_{oc}, J_{sc}, FF, and efficiency of 36 devices under AM 1.5G illumination (active area 0.16 cm^2).; (**b**) the perovskite device photograph for the module (25 cm^2) with an efficiency of about 15.1% (active area 11.25 cm^2). (**c**) shows the PCE efficiency of perovskite composed of NiO_x thin films that annealed at 500 °C for 1 h with deposit times: 20 s, 40 s, 60 s, and 80 s, respectively.

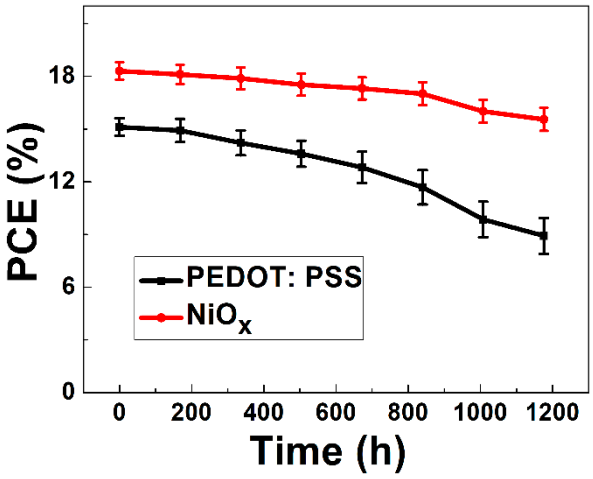

Figure 8. The long-term perovskite device stability fabricated for the PEDOT:PSS (black line) and NiO_x (red line) HTLs has been tested for 1200 h at 40% relative humidity (RH) and 25 °C.

4. Conclusions

In this research, our results strongly demonstrate a PVD processed with the high quality of NiO_x (thickness = 50 nm) films for HTL gives a high optical transmittance (>90%), good chemical stability, lower resistivity, and HOMO match perovskite ($CH_3NH_3PbI_3$) film layer. The performance of PSC explored here is an inverted (p-i-n structure) planar heterojunction perovskite solar cell with inorganic NiO_x HTL and C_{60} ETL structure. The structural stacking is given as FTO/NiO_x/$CH_3NH_3PbI_3$/C_{60}/BCP/Ag configuration. We produce about 36 devices of perovskite solar cells for repeatability tests. It was demonstrated PSC device with inorganic NiO_x HTL (thickness = 50 nm) gives about 1.2–1.8 times better durability than with an organic PEDOT:PSS HTL and the device owns the highest PCE is approximately 18.30% with active areas of the device are 0.16 cm^2 (under AM 1.5G illumination). In the module (25 cm^2), we demonstrate a perovskite device (active area 11.25 cm^2) with an efficiency of 15.1%.

Author Contributions: Conceptualization, C.-C.H. and C.-J.L.; Methodology, C.-C.H., S.-M.Y., K.-M.L. and C.-J.L.; Validation, C.-C.H., K.-M.L. and B.-Y.L.; Resources, S.-M.Y. and K.-M.L.; Writing—original draft preparation, C.-C.H.; Writing—review and editing, C.-C.H. and F.-R.C.; Supervision, F.-R.C. All authors have read and agreed to the published version of the manuscript.

Funding: This research was supported by the Ministry of Science and Technology, Taiwan (Grant Number: MOST 106-2218-E-182-005-MY2) and the Chang Gung Memorial Hospital, Linkou, Taiwan (CMRPD2G0301). FRC also would like to acknowledge the support from MOST-105-2221-E-007-023-MY3, MOST 104-2221-E-007-067-MY3, and the City University of Hong Kong under projects of project number 9360162 and 9380092.

Institutional Review Board Statement: Not applicable.

Informed Consent Statement: Not applicable.

Data Availability Statement: Not applicable.

Acknowledgments: We acknowledge the Ministry of Science and Technology, Taiwan (Grant Number: MOST 106-2218-E-182-005-MY2) and the Chang Gung Memorial Hospital, Linkou, Taiwan (CMRPD2G0301). FRC also would like to acknowledge the support from MOST-105-2221-E-007-023-MY3, MOST 104-2221-E-007-067-MY3, and the City University of Hong Kong under projects of project number 9360162 and 9380092.

Conflicts of Interest: The authors declare no conflict of interest.

References

1. Min, H.; Lee, D.Y.; Kim, J.; Kim, G.; Lee, K.S.; Kim, J.; Paik, M.J.; Kim, Y.K.; Kim, K.S.; Kim, M.G.; et al. Perovskite solar cells with atomically coherent interlayers on SnO_2 electrodes. *Nature* **2021**, *598*, 444–450. [CrossRef] [PubMed]
2. Sadegh, F.; Akin, S.; Moghadam, M.; Keshavarzi, R.; Mirkhani, V.; Ruiz-Preciado, M.A.; Akman, E.; Zhang, H.; Amini, M.; Tangestaninejad, S.; et al. Copolymer-Templated Nickel Oxide for High-Efficiency Mesoscopic Perovskite Solar Cells in Inverted Architecture. *Adv. Funct. Mater.* **2021**, *31*, 2102237. [CrossRef]
3. Akman, E.; Akin, S. Poly(*N*,*N*′-bis-4-butylphenyl-*N*,*N*′-bisphenyl)benzidine-Based Interfacial Passivation Strategy Promoting Efficiency and Operational Stability of Perovskite Solar Cells in Regular Architecture. *Adv. Mater.* **2021**, *33*, 2006087. [CrossRef] [PubMed]
4. Akman, E.; Shalan, A.E.; Sadegh, F.; Akin, S. Moisture-Resistant $FAPbI_3$ Perovskite Solar Cell with 22.25 % Power Conversion Efficiency through Pentafluorobenzyl Phosphonic Acid Passivation. *ChemSusChem* **2021**, *14*, 1176–1183. [CrossRef] [PubMed]
5. Ozturk, T.; Akman, E.; Shalan, A.E.; Akin, S. Composition engineering of operationally stable $CsPbI_2Br$ perovskite solar cells with a record efficiency over 17%. *Nano Energy* **2021**, *87*, 106157. [CrossRef]
6. Shalan, A.E.; Akman, E.; Sadegh, F.; Akin, S. Efficient and Stable Perovskite Solar Cells Enabled by Dicarboxylic Acid-Supported Perovskite Crystallization. *J. Phys. Chem. Lett.* **2021**, *12*, 997–1004. [CrossRef] [PubMed]
7. Jung, H.S.; Park, N.G. Perovskite solar cells: From materials to devices. *Small* **2015**, *11*, 10–25. [CrossRef]
8. Xing, G.; Mathews, N.; Sun, S.; Lim, S.S.; Lam, Y.M.; Grätzel, M.; Mhaisalkar, S.; Sum, T.C. Long-Range Balanced Electron- and Hole-Transport Lengths in Organic-Inorganic $CH_3NH_3PbI_3$. *Sci. Adv.* **2013**, *342*, 344–347. [CrossRef]
9. Bai, Y.; Yu, H.; Zhu, Z.; Jiang, K.; Zhang, T.; Zhao, N.; Yang, S.; Yan, H. High performance inverted structure perovskite solar cells based on a PCBM:polystyrene blend electron transport layer. *J. Mater. Chem. A* **2015**, *3*, 9098–9102. [CrossRef]

10. Liang, P.W.; Chueh, C.C.; Williams, S.T.; Jen, A.Y. Roles of Fullerene-Based Interlayers in Enhancing the Performance of Organometal Perovskite Thin-Film Solar Cells. *Adv. Energy Mater.* **2015**, *5*, 1402321. [CrossRef]
11. Yin, X.; Yao, X.; Luo, Q.; Dai, X.; Zhou, Y.; Zheng, Y.; Zhou, Y.; Luo, S.; Li, J.; Wang, N.; et al. High Efficiency Inverted Planar Perovskite Solar Cells with Solution-Processed NiO_x Hole Contact. *ACS Appl. Mater. Interfaces* **2017**, *9*, 2439–2448. [CrossRef]
12. Chang, S.H.; Lin, K.F.; Chiu, K.Y.; Tsai, C.L.; Cheng, H.M.; Yeh, S.C.; Wu, W.T.; Chen, W.N.; Chen, C.T.; Chen, S.H.; et al. Improving the efficiency of $CH_3NH_3PbI_3$ based photovoltaics by tuning the work function of the PEDOT:PSS hole transport layer. *Sol. Energy* **2015**, *122*, 892–899. [CrossRef]
13. Kim, S.K.; Seok, H.J.; Choi, D.H.; Nam, S.J.; Kim, S.C.; Kim, H.K. Comparison of NiO_x thin film deposited by spin-coating or thermal ecaporation for application as a hole transport layer of perovskite solar cells. *RSC Adv.* **2020**, *10*, 43847–43852. [CrossRef]
14. D'Amario, L.; Fohlinger, J.; Boschloo, G.; Hammarstrom, L. Unveiling hole trapping and surface dynamics of NiO nanoparticles. *Chem. Sci.* **2018**, *9*, 223–230. [CrossRef] [PubMed]
15. Hossain, M.I.; Shahiduzzaman, M.; Ahmed, S.; Huqe, M.R.; Qarony, W.; Saleque, A.M.; Akhtaruzzaman, M.; Knipp, D.; Tsang, T.H.; Taima, T.; et al. Near field control for enhanced photovoltaic performance and photostability in perovskite solar cells. *Nano Energy* **2021**, *89*, 106388. [CrossRef]
16. Hossain, M.I.; Shahiduzzaman, M.; Saleque, A.M.; Huqe, M.R.; Qarony, W.; Ahmed, S.; Akhtaruzzaman, M.; Knipp, D.; Tsang, Y.H.; Taima, T.; et al. Improved Nanophotonic Front Contact Design for High Performance Perovskite Single-Junction and Perovskite/Perovskite Tandem Solar Cells. *Sol. RRL* **2021**, *5*, 2100509. [CrossRef]
17. Hossain, M.I.; Saleque, A.M.; Ahmed, S.; Saidjafarzoda, I.; Shahiduzzaman, M.; Qarony, W.; Knipp, D.; Biyikli, N.; Tsang, Y.H. Perovskite/perovskite planer tandem solar cells: A comprehensive guideline for reaching energy conversion efficiency beyond 30%. *Nano Energy* **2021**, *79*, 105400. [CrossRef]
18. Muslih, W.Y.; Shahiduzzaman, M.; Akhtaruzzaman, M.; Hossain, M.I.; Wang, L.; Alkhammash, H.I.; Alharthi, S.S.; Nakano, M.; Karakawa, M.; Aminuzzaman, M. Reproducible perovskite solar cells using a simple solvent mediated sol−gel synthesized NiO_x hole transport layer. *Appl. Phys.* **2022**, 15, 015504. *Appl. Phys.* **2022**, *15*, 015504. [CrossRef]
19. Hossain, M.I.; Hasan, A.K.M.; Qarony, W.; Shahiduzzaman, M.; Islam, M.A.; Ishikawa, Y.; Uraoka, Y.; Amin, N.; Knipp, D.; Akhtaruzzaman, A.; et al. Electrical and Optical Properties of Nickel- Oxide Films for Efficient Perovskite Solar Cells. *Small Methods* **2020**, *4*, 2000454. [CrossRef]
20. Chen, W.; Liu, F.Z.; Feng, X.Y.; Djurišic´, A.; Chan, W.K.; He, Z.B. Cesium Doped NiO_x as an Efficient Hole Extraction Layer for Inverted Planar Perovskite Solar Cells. *Adv. Energy Mater.* **2017**, *7*, 1700722. [CrossRef]
21. Yan, W.; Ye, S.; Li, Y.; Sun, W.; Rao, H.; Liu, Z.; Bian, Z.; Huang, C. Hole-Transporting Materials in Inverted Planar Perovskite Solar Cells. *Adv. Energy Mater.* **2016**, *6*, 1600474. [CrossRef]
22. Li, M.H.; Shen, P.S.; Wang, K.C.; Guo, T.F.; Chen, P. Inorganic p-type contact materials for perovskite-based solar cells. *J. Mater. Chem. A* **2015**, *3*, 9011–9019. [CrossRef]
23. Chen, W.; Wu, Y.; Fan, J.; Djurišic´, A.; Liu, F.; Tam, H.W.; Ng, A.; Surya, C.; Chan, W.K.; Wang, D.; et al. Understanding the Doping Effect on NiO: Toward High-Performance Inverted Perovskite Solar Cells. *Adv. Energy Mater.* **2018**, *8*, 1703519. [CrossRef]
24. Jeng, J.Y.; Chen, K.C.; Chiang, T.Y.; Lin, P.Y.; Tsai, T.D.; Chang, Y.C.; Guo, T.F.; Chen, P.; Wen, T.C.; Hsu, Y.J. Nickel Oxide Electrode Interlayer in $CH_3NH_3PbI_3$ Perovskite/PCBM Planar-Heterojunction Hybrid Solar Cells. *Adv. Mater.* **2014**, *26*, 4107–4113. [CrossRef] [PubMed]
25. Corani, A.; Li, M.H.; Shen, P.S.; Chen, P.; Guo, T.F.; Nahhas, A.E.; Zheng, K.; Yartsev, A.; Sundström, V.; Ponseca, C.S., Jr. Ultrafast Dynamics of Hole Injection and Recombination in Organometal Halide Perovskite Using Nickel Oxide as p-Type Contact Electrode. *J. Phys. Chem. Lett.* **2016**, *7*, 1096–1101. [CrossRef]
26. Zhang, B.; Su, J.; Guo, X.; Zhou, L.; Lin, Z.; Feng, L.; Zhang, J.; Chang, J.; Hao, Y. NiO/Perovskite Heterojunction Contact Engineering for Highly Efficient and Stable Perovskite Solar Cells. *Adv. Sci.* **2020**, *7*, 1903044. [CrossRef]
27. You, J.; Meng, L.; Song, T.B.; Guo, T.F.; Yang, Y.; Chang, W.H.; Hong, Z.; Chen, H.; Zhou, H.; Chen, Q.; et al. Improved air stability of perovskite solar cells via solution-processed metal oxide transport layers. *Nat. Nanotechnol.* **2016**, *11*, 75–81. [CrossRef]
28. Yin, X.; Han, J.; Zhou, Y.; Gu, Y.; Tai, M.; Nan, H.; Zhou, Y.; Li, J.; Lin, H. Critical roles of potassium in charge-carrier balance and diffusion induced defect passivation for efficient inverted perovskite solar cells. *J. Mater. Chem. A* **2019**, *7*, 5666–5676. [CrossRef]
29. Kim, H.; Lee, J.; Ok, S.; Choe, Y. Effects of pentacene-doped PEDOT: PSS as a hole-conducting layer on the performance characteristics of polymer photovoltaic cells. *Nanoscale Res. Lett.* **2012**, *7*, 5. [CrossRef]
30. Ukoba, K.O.; Eloka-Eboka, A.E.; Inambao, F.L. Review of nanostructured NiO thin film deposition using the spray pyrolysis technique. *Renew. Sustain. Energy Rev.* **2018**, *82*, 2900–2915. [CrossRef]
31. Qiu, Z.; Gong, H.; Zheng, G.; Yuan, S.; Zhang, H.; Zhu, X.; Zhou, H.; Cao, B. Enhanced physical properties of pulsed laser deposited NiO films via annealing and lithium doping for improving perovskite solar cell efficiency. *J. Mater. Chem. C* **2017**, *5*, 7084–7094. [CrossRef]
32. Liu, Z.; Chang, J.; Lin, Z.; Zhou, L.; Yang, Z.; Chen, D.; Zhang, C.; Liu, S.; Hao, Y. High-Performance Planar Perovskite Solar Cells Using Low Temperature, Solution–Combustion-Based Nickel Oxide Hole Transporting Layer with Efficiency Exceeding 20%. *Adv. Energy Mater.* **2018**, *8*, 1703432. [CrossRef]
33. Zhong, Y.; Suzuki, K.; Inoue, D.; Hashizume, D.; Izawa, S.; Hashimoto, K.; Koganezawa, T.; Tajima, K. Interface-induced crystallization and nanostructure formation of [6,6]-phenyl-C61-butyric acid methyl ester (PCBM) in polymer blend films and its application in photovoltaics. *J. Mater. Chem. A* **2016**, *4*, 3335–3341. [CrossRef]

34. Hsu, C.C.; Yu, S.M.; Lee, K.M.; Lin, C.J.; Cheng, H.C.; Chen, F.R. Solid-state reaction process for high-quality organometallic halide perovskite thin film. *Sol. Energy Mater Sol. Cells* **2021**, *227*, 111014. [CrossRef]
35. Qarony, W.; Hossain, M.I.; Jovanov, V.; Salleo, A.; Knipp, D. Influence of Perovskite Interface Morphology on the Photon Management in Perovskite/Silicon Tandem Solar Cells. *ACS Appl. Mater. Interfaces* **2020**, *12*, 15080–15086. [CrossRef]
36. Hossain, M.I.; Hongsingthong, A.; Qarony, W.; Sichanugrist, P.; Konagai, M.; Salleo, A.; Knipp, D.; Tsang, Y.H. Optics of Perovskite Solar Cell Front Contacts. *ACS Appl. Mater. Interfaces* **2019**, *11*, 14693–14701. [CrossRef] [PubMed]
37. Hossain, M.I.; Khan, H.A.; Kozawa, M.; Qarony, W.; Salleo, A.; Hardeberg, J.Y.; Fujiwara, H.; Tsang, Y.H.; Knipp, D. Perovskite Color Detectors: Approaching the Efficiency Limit. *ACS Appl. Mater. Interfaces* **2020**, *12*, 47831–47839. [CrossRef]
38. Wheeler, S.; Deledalle, F.; Tokmoldin, N.; Kirchartz, T.; Nelson, J.; Durrant, J.R. Influence of Surface Recombination on Charge-Carrier Kinetics in Organic Bulk Heterojunction Solar Cells with Nickel Oxide Interlayers. *Phys. Rev. Appl.* **2015**, *4*, 024020. [CrossRef]
39. Jin, Z.; Guo, Y.; Yuan, S.; Zhao, J.S.; Liang, X.M.; Qin, Y.; Zhang, J.P.; Ai, X.C. Modification of NiOx hole transport layer for acceleration of charge extraction in inverted perovskite solar cells. *RSC Adv.* **2020**, *10*, 12289–12296. [CrossRef]